CrossMark

The Potential of Detecting Radio-flaring Ultracool Dwarfs at L band in the FAST Drift-scan Survey

Jing Tang[1], Chao-Wei Tsai[1], and Di Li[1,2,3]

[1] CAS Key Laboratory of FAST, National Astronomical Observatories, Chinese Academy of Sciences, Beijing 100101, China; jtang@nao.cas.cn, cwtsai@nao.cas.cn, dili@nao.cas.cn

[2] University of Chinese Academy of Sciences, Beijing 100049, China

[3] NAOC-UKZN Computational Astrophysics Centre, University of KwaZulu-Natal, Durban 4000, South Africa

Abstract

The Five-hundred-meter Aperture Spherical radio Telescope (FAST) completed its commissioning and began the Commensal Radio Astronomy FasT Survey (CRAFTS), a multi-year survey to cover 60% of the sky, in 2020. We present predictions for the number of radio-flaring ultracool dwarfs (UCDs) that are likely to be detected by CRAFTS. Based on the observed flaring UCDs from a number of unbiased, targeted radio surveys in the literature, we derive a detection rate of $\geqslant 3\%$. Assuming a flat radio spectrum $\nu L_\nu \propto \nu^{\beta+1}$ with $\beta = -1.0$ for UCD flares, we construct a flare luminosity function $dN/dL \propto L^{-1.96\pm0.45}$ (here $L = \nu L_\nu$). CRAFTS is found to be sensitive enough for flares from UCDs up to $\sim$180 pc. Considering the Galactic thin disk, we carry out a 3D Monte Carlo simulation of the UCD population, which is then fed to mock CRAFTS observations. We estimate that $\sim$170 flaring UCDs would be detected through transient searches in circular polarization. Though only marginally sensitive to the scale height of UCDs, the results are very sensitive to the assumed spectral index β. For β from 0 to -2.5, the number of expected detections increases dramatically from $\sim$20 to $\sim$3460. We also contemplate the strategies for following up candidates of flaring UCDs, and discuss the implications of survey results for improving our knowledge of UCD behavior at L band and dynamos.

Key words: surveys – (stars:) brown dwarfs – stars: flare – stars: low-mass – stars: magnetic field – radio continuum: stars

1. Introduction

Ultracool dwarfs (UCDs) include very low mass stars (spectral types $\geqslant$M7) and brown dwarfs (L, T and Y) (Kirkpatrick et al. 1999). Since the discovery of the unexpected radio emission from LP 944–20 (M9) in 2001 (Berger et al. 2001), more radio-active UCDs have been found. This radio emission is non-thermal and can be used as the magnetic activity indicator. For solar-type stars, magnetic fields are thought to depend on the shearing at the interface between the inner radiative zone and the outer convective envelope (Parker 1975). In contrast, UCDs are fully convective. How magnetic fields are generated and maintained in these objects is a big challenge to our understanding of dynamo processes. There are already many dynamo models (e.g., Browning 2008; Christensen et al. 2009; Yadav et al. 2015), and more observational evidences are needed to test these models. For earlier type stars, Hα emission from the chromosphere and X-ray emission from the corona are also used to indirectly trace the magnetic activity. However, these emissions decline significantly in UCDs (Gizis et al. 2000; Mohanty & Basri 2003; West et al. 2004; Berger et al. 2010; Williams et al. 2014; Schmidt et al. 2015), and thus are much less efficient probes in these objects.

Radio-active UCDs exhibit both flaring and quiescent (also known as persistent) radio emission. The flaring emission is thought to be caused by the electron cyclotron maser (ECM) instability (Hallinan et al. 2008; see Treumann 2006 for a review). Hallinan et al. (2015) further detected both radio and optical emissions powered by magnetospheric currents from LSR J1835+3259 (M8.5), confirming this coherent radio emission has the auroral origin as that from magnetized planets in solar system. Apart from the auroral origin which requires large-scale fields, this ECM flaring emission can be also produced in localized active regions (Treumann 2006; Lynch et al. 2015), similar to solar and stellar flares attributed to maser action. The ECM emission is highly circularly polarized (up to 100%) (Burgasser & Putman 2005; Hallinan et al. 2007, 2008; Antonova et al. 2008; Berger et al. 2009; Route & Wolszczan 2012; Williams et al. 2015a; Williams & Berger 2015; Route & Wolszczan 2016a) and rotationally modulated (Hallinan et al. 2006, 2007, 2008; Berger et al. 2009; Williams & Berger 2015; Kao et al. 2018). This emission is produced at the electron cyclotron fundamental frequency (Treumann 2006), $\nu_{\mathrm{MHz}} \approx 2.8 \times B_{\mathrm{Gauss}}$, and can be used to measure local magnetic field strengths. As the magnetic field on a UCD extends into a range

of heights over the surface, the bandwidth is then determined by the difference between the highest and lowest field strengths. Multi-frequency observations are needed to study the nature of the radio emission. The quiescent emission is considered to be gyrosynchrotron or synchrotron radiation from mildly or highly relativistic electrons (Hallinan et al. 2006; Williams et al. 2015b; Pineda et al. 2017).

Among the dynamo models for fully convective stars, Christensen et al. (2009) claimed convected energy flux determines the magnetic field strength and proposed a convection-driven dynamo scaling law for describing field strengths of rapidly rotating low-mass stars and planets. Based on that, Reiners et al. (2009) provided a semi-empirical method to estimate the field strengths of brown dwarfs and giant planets from their masses, radii, and luminosities. However, Kao et al. (2018) showed a clear departure of T dwarfs from this scaling law. They gave several possible explanations, such as higher-order non-dipole fields and age-evolving effect on magnetic energy. Yet the conclusions cannot be drawn with the small number of observed cases. More samples of late L and T dwarfs are needed to investigate the field topologies and the age dependence in dynamos. On the other hand, Kao et al. (2019) took pilot observations of three Y dwarfs with VLA at 4–8 GHz and failed to detect any pulsed radio emission. One possibility is that the observed frequency is too high, as the predicted field strengths for Y dwarfs are ∼hundreds of Gauss (Christensen et al. 2009), and the pulse caused by ECM should be lower than 4 GHz. Thus surveys at lower frequencies are crucial to search for new objects with weaker magnetic fields and shed light on convective dynamos.

The VLA Faint Images of the Radio Sky at Twenty-cm (FIRST; Becker et al. 1995) survey is a well-known 1.4 GHz survey with high sensitivity (∼0.15 mJy) and resolution (∼5″). This survey has a point-source detection threshold ∼1 mJy, while covering ∼10,000 deg². A comprehensive search for radio-active UCDs in the FIRST survey is not conducted. Although most known radio-active UCDs are outside the FIRST coverage, McLean et al. (2011) identified the persistent, non-flaring emission from 2MASS J13142039+1320011 in this survey. Another noticeable 1.4 GHz survey, the NRAO VLA Sky Survey (NVSS; Condon et al. 1998) covers the sky north of $\delta = -40°$, but the detection limit is ∼2.5 mJy, not sensitive enough to detect the predicted 1.4 GHz radio emission from UCDs. Recently, in the LOFAR Two-meter Sky Survey (LoTSS; Shimwell et al. 2017, 2019), Vedantham et al. (2020) discovered a T6.5 dwarf BDR J1750+3809, indicating that low-frequency radio surveys can discover substellar objects that are too cold and/or distant to be detected in current infrared surveys.

FAST, the largest single dish telescope in the world, will be able to efficiently investigate the radio-flaring UCDs at low frequencies (⩽1.4 GHz). The telescope finished its commissioning in early 2020. FAST has begun the Commensal Radio

Astronomy FasT Survey (CRAFTS; Li et al. 2018), which utilizes a novel and unprecedented mode to realize simultaneous data taking for pulsar search, Galactic H I mapping, H I galaxy study and transient FRB search. CRAFTS implements a high frequency CAL injection scheme, which facilitates the recovery of bandpass and the monitoring of polarization calibration.

We consider here the advantages and challenges of radio-flaring UCD detections through the CRAFTS survey. For FAST, the most significant problem is the severe confusion due to the large beam size. The highly circularly polarized nature of the radio flaring emission, in conjunction with a full polarization recording should improve significantly their detectability. Also, CRAFTS is designed to be a two-pass survey, the flux comparison between two epochs can be used to search for possible radio transients. Increasing radio-active UCD sample would advance our understanding of physical properties (e.g., age, rotation rate and bolometric luminosity) associated with magnetic activities in these objects.

In this paper, we provide the predictions on the potential of FAST to detect radio flares from UCDs. In Section 2, we investigate the flaring UCD detection rate, the radio luminosity function (LF) and the duty cycle of the flares, which are the necessary ingredients for the following simulation. In Section 3, we describe CRAFTS specifications and carry out the Monte Carlo simulation to explore the possibility of searching for flaring UCDs in CRAFTS. In Section 4, we consider the variation of each ingredient, including the spectral index of the flaring emission, in the simulation and their impact on the results. We also discuss the target selection strategy for follow-up observations, and the implication of flaring UCD search in CRAFTS. Finally we present our conclusions in Section 5.

2. Relevant Parameters

In this section, we summarize the radio-active UCDs detected in previous surveys from the literature, and assess the flaring UCD detection rate, construct the LF of the radio flares, and estimate the flare duty cycle. These parameters are kernels of the Monte Carlo simulation in Section 3.2 to predict the number of radio-flaring UCDs that could potentially be discovered in CRAFTS. Our simulation follows the methodology of Route (2017), yet includes more careful treatment to derive the radio LF of UCD flares based on the results of previous radio UCD surveys, though the sample is very small. The duty cycle and the temporal evolution of the flare which were overlooked in Route (2017) are also included.

2.1. Previous Surveys for Radio-active UCDs

Over the past two decades, a number of surveys have been carried out to search for radio-active UCDs, motivated by the first radio detection of LP 944–20 (Berger et al. 2001). Till

today, there are 26 detections of radio-emitting UCDs reported in the literature. The properties of these sources were summarized in Pineda et al. (2017), except VHS 1256-1257 (Guirado et al. 2018) and 2MASS J17502484-0016151 (Richey-Yowell et al. 2020).

Berger (2002) utilized VLA to observe 11 dwarfs ranging from M8 through T6 and detected flares and persistent emission from three sources. Burgasser & Putman (2005) monitored seven Southern late M and L dwarfs with ATCA at 4.80 and 8.64 GHz simultaneously, and two sources were found to exhibit radio emission, one of which is the most radio-luminous UCD to date, namely DENIS J1048-3956. Berger (2006) analyzed a large sample of 88 objects ranging from M7 to T8 observed by VLA, and found two sources showed quiescent emission. Osten & Jayawardhana (2006) observed three young UCDs (M8–M8.5) with no radio detection. Later McLean et al. (2012) conducted another survey with VLA, including 76 dwarfs of spectral types M7–L3.5, and detected radio emission from two UCDs. In addition, Phan-Bao et al. (2007) took VLA observations of eight UCDs in a narrow range of spectral type M8–M9.5 and found one more quiescent source. The aforementioned surveys were all conducted at 8.5 GHz. In order to search for UCDs capable of producing radio emission at lower frequencies, Antonova et al. (2008) attempted a mini-survey of eight dwarfs spanning from M8.5 to T6 with VLA at 4.9 GHz, contributing one new flaring source, while a later survey of 32 UCDs covering spectral type M7–T8 made no detection (Antonova et al. 2013). Moreover, Williams et al. (2014) observed five UCDs (M7.5–M9) with upgraded VLA centered at 5.0 and 7.1 GHz simultaneously, yielding one detection. Later Lynch et al. (2016) did a small ATCA survey of Southern 15 UCDs ranging from M7 to L8 centered at 5.5 and 9.0 GHz simultaneously, and found a new quiescent source. More recently, Zic et al. (2019) analyzed GMRT observations of nine UCDs (mainly L dwarfs) at around 1300 and 610 MHz, without any new detection. On the other hand, a pilot survey with VLA C-band targeting Hα-emitting and/or optical/IR variable dwarfs (L7–T6.5), achieved detection in four of five objects (Kao et al. 2016). This target selection strategy is based on the work of Hallinan et al. (2015) who suggested the highly circularly polarized radio emission has the same nature as the auroral emission from magnetic planets in the solar system and is driven by large-scale currents due to the magnetosphere-ionosphere coupling. Furthermore, Kao et al. (2019) observed three known IR-variable Y dwarfs, but without any new detection. Richey-Yowell et al. (2020) made a survey of 17 photometrically variable brown dwarfs with VLA at 4–8 GHz, and found one more source with both quiescent and flaring emissions. In addition, there were several other radio-detected UCDs in the targeted observations (Burgasser et al. 2013; Gizis et al. 2013; Burgasser et al. 2015; Osten et al. 2015; Gizis et al. 2016; Guirado et al. 2018).

Apart from interferometers, Arecibo was also used to study radio-flaring UCDs. Route & Wolszczan (2013) initially led the 4.75 GHz Arecibo survey of 33 objects spanning spectral range M9–T9, and discovered the first radio-emitting T dwarf. Another flaring T dwarf was detected in the second survey of 27 UCDs encompassing spectral type M7–T9 (Route & Wolszczan 2016b).

In total, 26 out of 269 observed UCDs, including a few that were surveyed more than once, were detected as radio emitters, yielding an overall detection efficiency of ∼10%. It is worth noting that the biased survey in Kao et al. (2016) guided by auroral activity tracers such as Hα emission and/or optical/IR variability seems to be efficient. However, other optical Hα surveys may also result in low detection rate. For example, Pineda et al. (2016) conducted an optical spectroscopic survey of L and T dwarfs with the Keck telescopes and achieved an Hα detection rate of ∼9.2%, statistically equivalent to that of the radio surveys aforementioned. Another thing we would like to point out is that BDR J1750+3809 discovered in LoTSS (Vedantham et al. 2020) is the only radio-active brown dwarf reported in that blind survey so far, and the detection rate is unknown. Hence we do not consider this object in the following statistical analysis.

2.2. Detection Rate of Radio-flaring UCDs from Unbiased Surveys

As FAST is sensitive to rapidly varying radio emission, here we have only estimated the detection rate of flaring UCDs from those unbiased, targeted surveys since 2002 (Berger 2002, 2006; Burgasser & Putman 2005; Phan-Bao et al. 2007; Antonova et al. 2008, 2013; McLean et al. 2012; Route & Wolszczan 2013, 2016b; Williams et al. 2014; Lynch et al. 2016; Zic et al. 2019). Here the term "unbiased" means that the targets are selected without preferences, e.g., rotation, age, or X-ray and Hα activity, which are thought to be associated with the radio activity. These surveys were carried out using different observation modes, however, because they are sensitive to several-minute-long flares, we still combine these results for statistical analysis. In these surveys, a total of 236 UCDs of spectral types M7-T9 were observed, and seven radio-flaring dwarfs were detected (see Table 1), yielding a detection rate of ∼3%.

Flaring UCDs cannot be always identified in the surveys, e.g., LSR J1835+3259 and 2MASS J1314+1320. The quiescent emission was initially detected from these objects in Berger (2006) and McLean et al. (2012), and then follow-up observations confirmed the occurrence of flares (Hallinan et al. 2008; Williams et al. 2015a). This may be due to insufficient observing time. Another possibility is the change of radio emission properties, which are related to magnetic structures, e.g., solar-like activity cycles originated from magnetic reversals (Route 2016) may cause flaring UCDs to undergo low magnetic activity periods. The low detection rate can be also caused by

Table 1
UCDs with Radio Flares from Unbiased Surveys

Object	SpT	d (pc)	$[L_{bol}]$ $L_\odot$	ν_{obs} (GHz)	$t_{on-source}$ (ks)	τ_{flare} (min)	$F_{\nu,R}$ (mJy)	νL_ν (10^{24} erg s^{-1})	Period (hr)[a]	Size	References[b]
J1048-3956[c]	M8.5	4.05 ± 0.002	-3.51	4.80	36	4–5[d]	6.00 ± 0.90	0.57 ± 0.08	...	7	14, 10, 9, **6**
				8.64	36	4–5[d]	29.00 ± 1.00	4.92 ± 0.17			
TVLM 513-46	M8.5	10.70 ± 0.02	-3.57	8.46	6.6	13.8[e]	0.89 ± 0.09	1.03 ± 0.10	1.96	12	15, 10, 9, **2**, _11_
J0024-0158[c]	M9.5	12.51 ± 0.03	-3.44	8.46	5.5	5.6[e]	0.33 ± 0.09	0.52 ± 0.14	...	12	18, 10, 9, **2**
J0746+2000B[c,f]	L1.5	12.36 ± 0.12	-3.77	4.90	5.4[g]	3.4[h]	1.60 ± 0.30[h]	1.43 ± 0.27	2.07	8	5, 8, 13, **1**, _3_
J0036+1821[c]	L3.5	8.74 ± 0.02	-3.93	8.46	9.6	21.5[e]	0.54 ± 0.10	0.42 ± 0.08	3.08	12	16, 10, 9, **2**, _12_
J1122+2550[c]	T6	17.72 ± 1.59	-4.90	4.75	7.2	2.0[i]	1.50 ± 0.20[j,k]	2.68 ± 0.60	...[l]	20[m]	17, 4, 19, **21**, _22_
J1047+2124[c]	T6.5	10.56 ± 0.42	-5.30	4.75	3.6	0.8	2.70 ± 0.20[j]	1.71 ± 0.19	1.77	31[n]	7, 23, 9, **20**, _24_

Notes. The columns are (left to right) (1) object name; (2) spectral type; (3) distance; (4) bolometric luminosity; (5) observing frequency; (6) total on-source observing time; (7) flare duration; (8) peak flux density; (9) radio luminosity; (10) period; (11) the size of the observed UCD sample in the survey; (12) references.
[a] The periods are obtained from the radio data.
[b] The references in sequence denote the source for the spectral type, the distance, and the bolometric luminosity. The radio survey and period references are in bold and underlined, respectively.
[c] The full names of these objects are, in table order, DENIS J1048.03956, 2MASSI J0024246015819, 2MASSI J0746425+200032, 2MASS J00361617+1821104, WISEP J112254.73+255021.5, and 2MASS J10475385+2124234.
[d] These two flares were detected at 4.8 GHz and 8.46 GHz simultaneously, with ∼10 minutes apart.
[e] These values are flare FWHM duration. For other sources in the table, the flare timescale is determined when the envelope of the flare departs from the background emission.
[f] J0746+2000 is an L0+L1.5 binary system (Bouy et al. 2004). The detected period of the radio pulses is consistent with that of the secondary L1.5 dwarf (Berger et al. 2009; Zhang et al. 2020). Note that the primary is also radio emitter (Zhang et al. 2020).
[g] This value is calculated according to the archive data at https://archive.nrao.edu/archive/advquery.jsp.
[h] The flux and duration correspond to the burst at 4.6 h in the light curve with 10 s time resolution (Antonova et al. 2008). The duration is calculated when the envelope of the burst departs from the value of the quiescent component, ∼0.2 mJy.
[i] The duration of the pulse is not clearly given in Route & Wolszczan (2016a), but it mentioned the detected pulses were 30–120 s. We choose 120 s as the duration of the first discovered flare according to its light curve.
[j] There are multiple pulses recorded in the follow-up observations after the initial discovery of this flaring brown dwarf. For the purpose of selecting the unbiased flare measurement as the representation of the radio luminosity of this source, we use the flux detected in the original discovery.
[k] The uncertainty is not clearly given in Route & Wolszczan (2016a). As the observations were carried out in the same way as Route & Wolszczan (2013), we adopt the same uncertainty.
[l] Route & Wolszczan (2016a) proposed a period of ∼17.3 minutes, while Williams et al. (2017) inferred the period of ∼116 minutes.
[m] In the survey of 27 brown dwarfs, 20 are not-previously observed targets by Arecibo.
[n] In the survey of 33 brown dwarfs, TVLM 513-46 and J0746+2000are included as calibration sources.

References. (1) Antonova et al. (2008), (2) Berger (2002), (3) Berger et al. (2009), (4) Best et al. (2018), (5) Bouy et al. (2004), (6) Burgasser & Putman (2005), (7) Burgasser et al. (2006), (8) Dupuy & Liu (2017), (9) Filippazzo et al. (2015), (10) Gaia Collaboration et al. (2018), (11) Hallinan et al. (2007), (12) Hallinan et al. (2008), (13) Harding et al. (2013), (14) Henry et al. (2004), (15) Kirkpatrick et al. (1995), (16) Kirkpatrick et al. (2000), (17) Kirkpatrick et al. (2011), (18) Leggett et al. (2001), (19) Pineda et al. (2017), (20) Route (2013), (21) Route & Wolszczan (2016a), (22) Route & Wolszczan (2016b), (23) Vrba et al. (2004), (24) Williams & Berger (2015).

other observational selection effects. For example, only when the beamed radio emission sweeps in the direction of the Earth during one rotation period of an object, it can be detected. Thus those with long rotational periods have much lower chances to be detected. Additionally, previous work focused on radio observations at ∼5 GHz and ∼8 GHz. That means objects with field strengths lower than ∼1.5 kGauss cannot be detected if ECM mechanism operates. On the other hand, this number may imply that radio inactive dwarfs occupy a large proportion, owing to the absence of either the magnetic field or the electrodynamic engine (e.g., satellite-induced, similar to Jupiter-Io system) to generate the radio emission (Hallinan et al. 2015; Kao et al. 2016; Pineda et al. 2017).

It is worth noting that in the radio surveys of UCDs with interferometers, Berger (2006), Phan-Bao et al. (2007), Antonova et al. (2013), Williams et al. (2014) and Lynch et al. (2016) searched for variability (flares) just for the objects that were detected in the images, and McLean et al. (2012) only examined the images for all sources. This could potentially introduce an issue of lower detection rate due to the flux dilution. When a flare with duration Δt occurs in the observation of time T ($\Delta t < T$), the signal-to-noise ratio (SNR) for the flare would be higher than that for the entire observation. We take the observation of TVLM 513-46 in Hallinan et al. (2007) as an example. Referring to the phase-folded light curve at 8.44 GHz (see Figure 3 in Hallinan et al. 2007), a single burst lasts for ∼8 minutes with the peak flux of ∼4 mJy, and the mean flux over a period of 1.958 h is 0.464 mJy. The rms noise grows with $time^{1/2}$, while the signal grows with *time*. Thus the SNR of the burst ($\propto 4 \times 8/\sqrt{8}$) exceeds the SNR of the duration of one

rotation period ($\propto 0.464 \times 1.958 \times 60/\sqrt{1.958 \times 60}$) by a factor of ~ 2.2. Here we use the peak flux instead of the average flux of the burst over the ~ 8 minutes, and the resultant value would be slightly larger. Antonova et al. (2008) reexamined the X band data in Hallinan et al. (2007) and obtained the value of 1.5. Note that if the quiescent emission is very low or absent, then the SNR of the burst over the whole observation would be diluted by a factor of $(\Delta t/T)^{1/2}$. Further, for the radio detection determined from the image, light curve needs to be constructed to search for the variability to confirm the fidelity of the flaring event (e.g., McLean et al. 2012, for J0952219–192431). Thus, if only synthesized interferometric images were made to search for radio emission without time series analysis, flares may be missed. With this concern in mind, we consider $\sim 3\%$ as a lower limit of the detection rate. As there is no obvious evidence that the detection rate changes across spectral types (Route & Wolszczan 2016b), we use a single rate 3% for all types of UCDs in the simulation.

2.3. Radio Luminosity Function of UCD Flares

In this section, we build a sample to derive the L-band LF of UCD flares. We combine the results from previous small size surveys, and establish a uniform standard to recalculate the flux densities of the flaring events from these inhomogeneous surveys.

For the radio flares of UCDs—J1048-3956, TVLM 513-46, J0024-0158, J0746+2000 and J0036+1821—that were first detected by interferometers, the peak flux densities are adopted directly from the light curves in the literature (Berger 2002; Burgasser & Putman 2005; Antonova et al. 2008). The median of the data outside the flare periods is calculated as the quiescent component, and the median absolute deviation of these data is then converted to the standard deviation to be considered as the flux uncertainty. The difference between the peak flux and the quiescent component is treated as the pure flare flux, and is used to construct the flare LF. We note that, for J1048-3956, the quiescent component, shown in Figure 3 of Burgasser & Putman (2005), is estimated as 0.53 mJy at 4.80 GHz and 0.64 mJy at 8.64 GHz, while it is 0.14 mJy at 4.80 GHz and <0.11 mJy at 8.64 GHz reported in the literature. This difference is likely due to that the observation is 12 h long, while the light curves provided in the literature were only for half an hour. For the case of J0746+2000, a series of bursts at 4.3 hr (two peaks), 4.5 h, 4.6 h and 4.9 h are seen in the light curve, which is shown in top-left panel of Figure 2 in Antonova et al. (2008). Here the median of these burst fluxes as the peak is adopted. For the detection of TVLM 513-46, J0024-0158 and J0036+1821 in Berger (2002), the time resolution in their light curves is 5.5 minutes, 8 minutes and 6.5 minutes, respectively. These large time bins may exceed the timescale of a single flare. For sources J1122+2550 and J1047+2124, they were first detected by Arecibo, and the quiescent emission

could not be distinguished from those observations. The follow-up VLA observations, however, showed the quiescent emission of these two objects is two orders of magnitude fainter than their flares (Williams et al. 2013; Williams & Berger 2015; Williams et al. 2017), and thus the weak quiescent flux is neglected. The summary of these results are presented in Table 1.

These flares were detected at ~ 5 GHz or ~ 8 GHz. In this work we assume the flux density spectra is $S_\nu \propto \nu^\beta$ with $\beta = -1.0$. This is equivalent to the assumption of a flat νL_ν for the flaring emission at different frequencies. Detailed discussion on the spectral index of the flaring emission can be found in Section 4.1.3. We then assume the LF follows a power-law distribution,

$$dN = kL^{-\alpha}dL, \tag{1}$$

where dN is the number of flares with radio luminosity between L and $L+dL$ (here $L = \nu L_\nu$), k is the normalization constant, and α is the power-law index.

In fact, $dN/dL = kL^{-\alpha}$ is the probability density function of L, denoted by $p(L)$. We follow the recipe laid out in Clauset et al. (2009) and estimate α using the method of *maximum likelihood*. We write down the log-likelihood function,

$$\ln \mathcal{L}(\alpha) = n \ln k - \alpha \sum_{i=1}^{n} \ln L_i, \tag{2}$$

with the normalization constant $k = (\alpha - 1)L_{\min}^{\alpha-1}$ for $\alpha > 1$. Here $L_{\min}$ is the lower bound on the peak luminosities of radio flares. As mentioned in Section 2.2, 236 UCDs were observed in unbiased, targeted radio surveys, and seven flaring objects were detected with the minimal radio luminosity of 4.2×10^{23} erg s^{-1}. In the remaining objects, about three-quarters have the detection limit below this luminosity. For a given LF with a positive α, the chance of detecting flares with lower luminosities should be higher, yet there is no detection. Thus here we set $L_{\min} = 4.2 \times 10^{23}$ erg s^{-1}. By maximizing Equation (2), α can be derived (Clauset et al. 2009),

$$\alpha = 1 + n \left[\sum_{i=1}^{n} \ln \frac{L_i}{L_{\min}} \right]^{-1}. \tag{3}$$

With our sample of flaring events reported in Table 1, we obtain $\alpha = 1.96$.

It is worth noting that the derived LF suffers from the small sample size significantly. However, this is the best sample available from all published literatures so far. Clauset et al. (2009) discussed the uncertainty of α derived from small sample in Appendix B, that is, $\sigma_\alpha = n(\alpha - 1)/(n - 1)\sqrt{n - 2}$. When n is large, $\sigma_\alpha = (\alpha - 1)/\sqrt{n}$. In our case, $\sigma_\alpha = 0.45$. The LF can be determined more accurately when more samples are available. The power-law fits with different parameters to the data are shown in Figure 1. We also consider the impact of measurement uncertainties of L on α. Then the
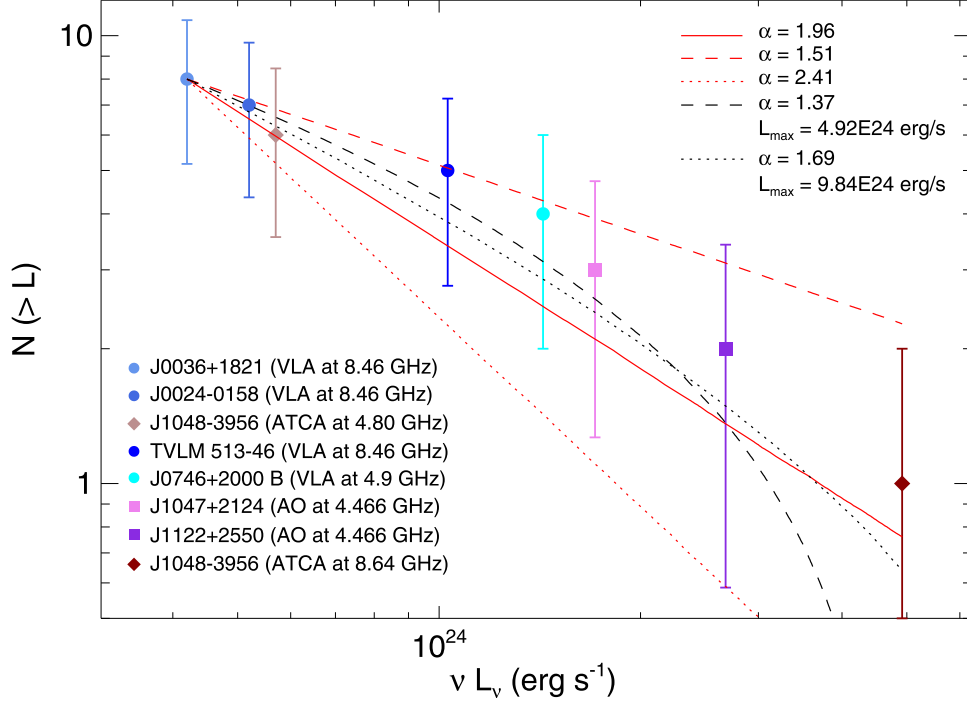
Figure 1. The power-law fits to the cumulative distribution of flaring events listed in Table 1. The expected uncertainty of the cumulative distribution is $\sigma_{\mathrm{cum},i} = \sqrt{N_i}$ (Aschwanden 2015). The power laws are $\alpha = 1.96$ (red solid line), $\alpha = 1.51$ (red dashed line), $\alpha = 2.41$ (red dotted line), $\alpha = 1.37$ with $L_{\max} = 4.92 \times 10^{24}$ erg s^{-1} (black dashed line) and $\alpha = 1.69$ with $L_{\max} = 9.84 \times 10^{24}$ erg s^{-1} (black dotted line). The latter two cases with high luminosity cutoff are discussed in Section 4.1. The lower bound $L_{\min} = 4.2 \times 10^{23}$ erg s^{-1} is set for all power laws.

probability density function of L is $p(L) = k/(\sqrt{2\pi}\,\sigma_L)$ $\int_{L_{\min}}^{\infty} x^{-\alpha} \exp(-(x - L)^2/2\sigma_L^2)dx$. To maximize the log-likelihood function, we obtain the numerical solution $\alpha = 1.98$. Thus this impact is negligible. In our simulation, we use the LF $dN/dL \propto L^{-1.96}$ with $L_{\min} = 4.2 \times 10^{23}$ erg s^{-1}. The uncertainty of α is also considered in the simulation (Section 3.2).

2.4. Rotation Periods, Flare Duty Cycle and Temporal Evolution

The flaring radio emission is shown to be rotationally modulated (Hallinan et al. 2006, 2007, 2008; Berger et al. 2009; Williams & Berger 2015; Kao et al. 2018). It is thus necessary to specify the distribution of rotation periods for the modeled UCD population. Radigan et al. (2014) assumed a lognormal period distribution in the form of

$$f(P) = \frac{1}{P\sigma_0\sqrt{2\pi}}e^{-\frac{(\ln P - \mu_0)^2}{2\sigma_0^2}}, \qquad (4)$$

where P is the period in hours, and the parameters $\mu_0 = 1.41$ and $\sigma_0 = 0.48$ are determined based on the previous $v\sin i$ studies of L and T dwarfs (Zapatero Osorio et al. 2006; Reiners & Basri 2008). Route (2017) reckoned the objects with rotation periods of $\leqslant 1$ h and $\geqslant 10$ h may be underestimated (Route & Wolszczan 2016a; Metchev et al. 2015), and suggested

$\mu_0 = 1.22$ and $\sigma_0 = 0.49$. However, for WISEPC J112254.73 +255021.5, in contrast to the period of 17.3 minutes given in Route & Wolszczan (2016a); Williams et al. (2017) inferred a longer period of 116 minutes. Since there is no further discussion on the parameter issue as claimed in Route (2017), here we adopt $\mu_0 = 1.41$ and $\sigma_0 = 0.48$.

The duty cycle is defined as the ratio of the flare duration to the rotation period. Here the flare duration is determined when the envelope of the flare departs from the background emission. Among the objects with confirmed periodic pulsations, the duty cycle is $\sim 35\%$ for TVLM 513-46 (Hallinan et al. 2007, multiple pulses with the most luminous one at X band lasting ~ 8 minutes), $\sim 12\%$ for LSR J1835+3259 (Hallinan et al. 2008, ~ 20 minutes flare), $> 30\%$ for 2MASS J0036+1821 (Hallinan et al. 2008, > 55 minutes flare), $\sim 0.8\%$ for 2MASS J0746+2000 (Berger et al. 2009, ~ 1 minutes flare), $\sim 20\%$–35\% for 2MASS J1314+1320 (Williams et al. 2015a, multiple 10^2–10^3 s flares), and $\sim 7.8\%$–12.6\% for 2MASS J1047+2124 (Williams & Berger 2015, ~ 500–800 s flare). Note that Berger (2002) measured the duty cycle of TVLM 513-46 to be $\tau_{\mathrm{flare}}/t_{\mathrm{on-source}} \approx 13\%$ (see Table 1). Apart from the diverse definition of the flare duration and duty cycle, the low time resolution of 5.5 minutes in Berger (2002) may smooth the weak and short-timescale variability, resulting in a different value of duty cycle. For the case of 2MASS J1047+2124, Route & Wolszczan (2012) detected sporadic radio bursts,

while Williams & Berger (2015) and Allers et al. (2020) measured a periodicity of $\sim$1.76 h. One possibility is that the sensitivity of Arecibo observations in Route & Wolszczan (2012) is $\sim$0.2 mJy, lower than $\sim$0.09 mJy in Williams & Berger (2015). The majority of flares observed in Williams & Berger (2015) and Allers et al. (2020) are below $\sim$0.6 mJy (3σ detection for Arecibo). Hence Route & Wolszczan (2012) would miss these weaker flares. Meanwhile, the lower sensitivity would shorten the flare timescales according to our definition. As the sensitivity of FAST observations is better than that in Williams & Berger (2015) (discussed in Section 3.1), we adopt the duty cycle of 2MASS J1047 +2124 in Williams & Berger (2015). It is worth noting that the different duty cycles measured for one object can also be caused by the intrinsic variation of flares. Based on light travel-time arguments, the flare duration is related to the extension of the source region where ECM emission generates by multiplying the velocity of light (Treumann 2006). A long flare timescale reflects an extended source region, and multiple pulses indicate several compact source regions. If the source region size changes, the flare duration and consequently the duty cycle would be changed. Considering the existing data are sparse to characterize the distribution of duty cycles, we simply assume a uniform distribution over the range from 0.8% to 35% in our simulation. That is, a random value of duty cycle in this range would be assigned to a modeled UCD each time, and the duty cycle variability would be taken into account in the performance of one thousand trials.

To describe the temporal evolution of the flare, we model the flare by exponentials with the same rise and decay time τ, that is, $F(t) = F_0 e^{(t-t_0)/\tau}$ for $t < t_0$ and $F(t) = F_0 e^{(t_0-t)/\tau}$ for $t > t_0$, where F_0 is the peak flux density at t_0. By modeling the flares of TVLM 513-46 in Hallinan et al. (2007), LSR J1835 +3259 in Hallinan et al. (2008) and 2MASS J0746+2000 in Berger et al. (2009), we choose 1 percent of the peak flux density as the cutoff of the exponentials, and then $\tau = -0.5 \times$ *flare duration*$/ \ln(0.01)$. Thus for a flare, when the peak flux density, the rotation period and the duty cycle are given, the profile can be shaped.

3. Search for Radio-flaring UCDs in CRAFTS

CRAFTS, as introduced in Section 1, is a large-scale commensal survey designed to observe extra-galactic H I, Galactic H I, pulsars and FRBs simultaneously using drift scans. Details on the survey can be referred to Li et al. (2018). Here we will discuss the possibility of utilizing the survey data for radio-flaring UCD search.

3.1. Basic Characteristics of CRAFTS

FAST is located at (106°.9 E, 25°.7 N) with a decl. range between $-14°.3$ and 65°.7, i.e., the maximum zenith angle (ZA) is $40°$ (Li et al. 2018). CRAFTS plans to carry out a two-pass

survey with one-pass completion of $\sim$220 full days, covering $\sim$23,000 deg^2, approximately 60% of the whole sky (Li et al. 2018). During the survey, FAST uses *L*-band Array of 19-beam (FLAN) receiver with a rotation of 23°.4 to achieve a super-Nyquist sampling (Li et al. 2018). The spacing between two adjacent drift scans is 21′.9 in decl. FLAN covers a 400 MHz bandpass centered at 1250 MHz. When ZA is below 26°.4, a fully 300 m aperture is illuminated, and the beam size is approximately 3′.7 at 1050 MHz and 2′.9 at 1450 MHz. The antenna gain is $\sim$16.5 K Jy^{-1}, and the system temperature increases with ZA from $\sim$18 K to $\sim$21 K at around 1250 MHz when $ZA < 26°.4$. (Jiang et al. 2019).

Zhang et al. (2019) estimated the FLAN beam size (θ), gain (G) and system temperature (T_{sys}) during the drift-scan observations, based on the FAST commissioning performance analysis from Jiang et al. (2019). When a point source drifts through the FLAN at a speed of v_s/arcmin s$^{-1} = 0.25 \times$ cos(decl.), it would be seen by several beams. We use a 2D Gaussian to describe the beam response to a point source. By doing a numerical experiment, we calculate the equivalent integration time, convolved with the Gaussian response curve, for each beam at 1450 MHz and add up all the time as the effective integration time (t_{eff}). In Figure 2, we show that t_{eff} ranges from $\sim$17 s at the equator to $\sim$60 s at the maximum decl. of 65°.7. The longer t_{eff} is due to the projection effect at high decl., and the increasing beam size due to partially-illuminated aperture at $ZA > 26°.4$. It is worth noting that there are gaps between beams and the total time drifting through a point source is approximately $2t_{eff}$.

In FLAN, dual-linear polarizations are available for each beam. The rms noise in a single polarization can be estimated by

$$\sigma = \frac{T_{sys}}{G}\frac{1}{\sqrt{t_{eff}\Delta\nu}}, \qquad (5)$$

$\Delta\nu$ is the bandwidth, and we use the full range 400 MHz, deducting 20% bandwidth loss due to RFI based on experience. The rms noise in Stokes V (σ_V) is $\sqrt{2}$ times larger than that in a single polarization (see Figure 3). The system temperature increases as a function of ZA and the gain drops off when $ZA > 26°.4$ due to the partially-illuminated aperture. The variation of σ_V with the decl. results from the competition of the effects of different parameters.

Stokes V suffers little confusion, and for linear polarization feeds, Stokes V is independent of gain fluctuation of the system when the two polarization paths are well isolated (Heiles 2001). Thus the measurement of Stokes V is a good method to search for flares. The processing of Stokes V data refers to the RHSTK package.[4] The gain and phase response of the system can be
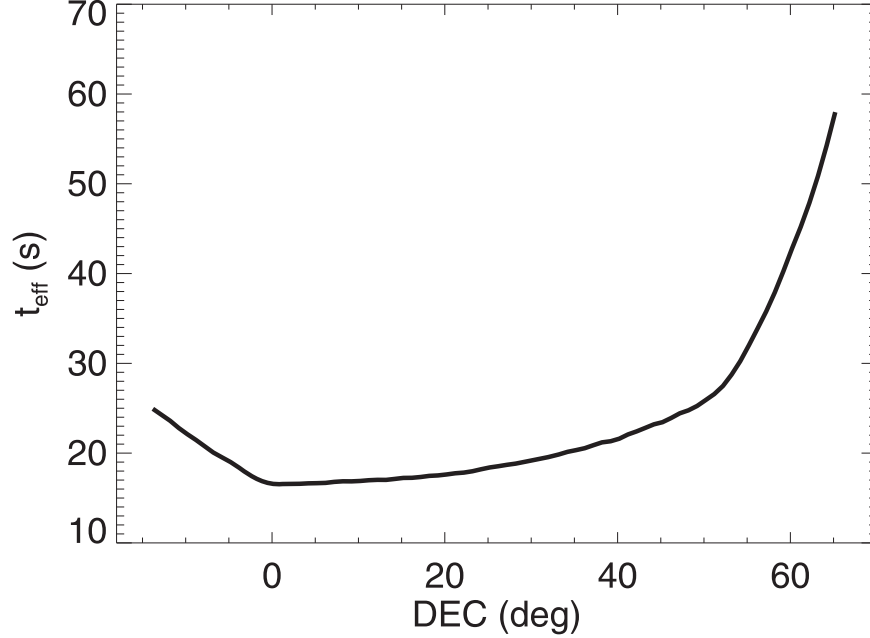
Figure 2. The effective integration time for CRAFTS one-pass drift scan as a function of decl. at $\nu = 1450$ MHz.

calibrated by the noise diode (CAL). For simplicity, the instrumental contribution to polarimetry is described using a unitary matrix, in which only zeroth-order effects are considered (Heiles et al. 2001). In this case the uncertainty of Stokes V due to the leakage of other Stokes parameters, mainly Stokes I, can be up to $\sim 10\%$. Thus only the detection of radio emission with circular polarization $>10\%$ is reliable. It is acceptable for flaring UCD search, as ECM emission is highly circularly polarized. Higher precision polarimetry is available when more corrections are made to remove the leakage of other Stokes parameters to Stokes V. Yet it is beyond the scope of this paper.

3.2. Mock UCD Catalog Generation

In this section, we describe the Monte Carlo simulation for generating mock catalog, and discuss how the flaring radio luminosity and distance are assigned to each source for FAST detection assessment.

In Table 1, DENIS J1048-3956 is found to have the most luminous flare with $\nu L \nu = 4.92 \times 10^{24}$ erg s^{-1}. This luminosity can be detected with $\geqslant 5\sigma_V$ by CRAFTS at 1250 MHz at a distance up to ~ 180 pc (see Figure 4), though this object itself is out of FAST sky coverage. In comparison, the scale height of low-mass stars in the Galactic thin disk is ~ 300 pc (Jurić et al. 2008; Pirzkal et al. 2009; Bochanski et al. 2010). To count the total number of all (radio emitting or not) UCDs within this distance, we consider the space density of UCDs. The local density of UCDs is calculated based on the compiled results from a number of volume-limited (<25 pc) surveys. The space

density is $\sim 11.1 \times 10^{-3}$ pc^{-3} for M7–L4 dwarfs (Bardalez Gagliuffi et al. 2019), $\sim 3.4 \times 10^{-3}$ pc^{-3} for L5–T5.5 dwarfs (Reylé et al. 2010), $>14.6 \times 10^{-3}$ pc^{-3} for T6 and later dwarfs with $T_{\rm eff} < 1050$ K (Kirkpatrick et al. 2019). These numbers have been accounted for the completeness. We follow the similar treatment in Route (2017) to sum up these objects of different spectral types to obtain a total space density of $>2.9 \times 10^{-2}$ pc^{-3} for UCDs.

Here we only consider the thin disk contribution for UCD space density

$$\rho = \rho_0 e^{-\frac{|Z|-Z_\odot}{H}}, \qquad (6)$$

where ρ_0 is the local density, Z is the vertical distance from the plane, and H is the scale height. We adopt $\rho_0 = 2.9 \times 10^{-2}$ pc^{-3} as discussed above, $Z_\odot = 15$ pc as the Galactic height of the Sun (Cohen 1995; Ng et al. 1997; Binney et al. 1997), and $H = 300$ pc as the scale height for UCDs (Jurić et al. 2008; Pirzkal et al. 2009; Bochanski et al. 2010). The influence of different scale heights to our estimates will be discussed later in Section 4.1.1. The Galactic height (Z) of each point is calculated by the equation given in Bochanski et al. (2010):

$$Z = Z_\odot + d \sin(b - \arctan(Z_\odot/R_\odot)), \qquad (7)$$

where d is the distance, b is the Galactic latitude. $R_\odot = 8.5$ kpc is taken as the Galactic radius of the Sun (Kerr & Lynden-Bell 1986). We note that the scale length of the thin disk is ~ 3 kpc, significantly larger than the distance of a few hundred pc we consider here for CRAFTS (as shown in Figure 4), so the
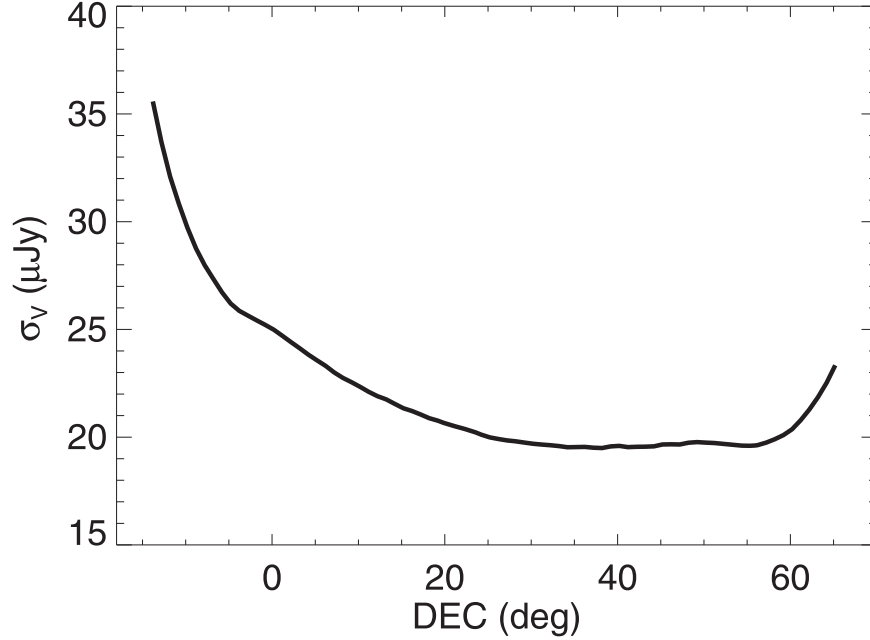
Figure 3. The rms noise in Stokes *V* for CRAFTS one-pass drift scan as a function of decl.. 320 MHz-bandwidth is used. The integration time is shown in Figure 2.
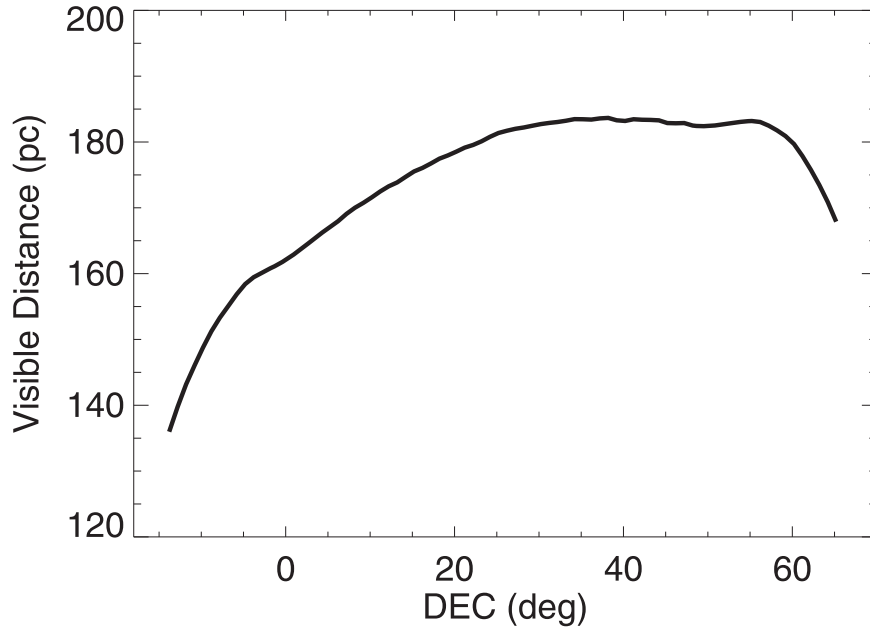

Figure 4. The visible distance of DENIS J1048-3956 flare with $\nu L\nu = 4.92 \times 10^{24}$ erg s^{-1} for CRAFTS one-pass drift scan as a function of decl. at $\nu = 1250$ MHz.

density variation along the radial direction is ignored in our calculation.

We sample the solar ambient space into small volume elements by each α (R.A.), δ (decl.), d bin, $\Delta\alpha = 1°$, $\Delta\delta = 1°$, $\Delta d = 5$ pc, marked with (α, δ, d). The UCD density ρ (α, δ, d) of each volume element is estimated based on Equation (6), after converting the center coordinates of the volume element from the equatorial coordinates (α, δ) to the galactic

coordinates (l, b) and further to the cylindrical coordinates (R, Z). An azimuthal symmetry of the Galactic disk (Jurić et al. 2008) is assumed. Multiplied by the individual volume size, we obtain the UCD number in each volume element N (α, δ, d), and then integrate over α to obtain N (δ, d). In a given δ, d bin, we generate N (δ, d) uniformly distributed random numbers, and then sum over d up to the farthest visible distance related to δ, denoted by N (δ). These artificial sources are given the radio
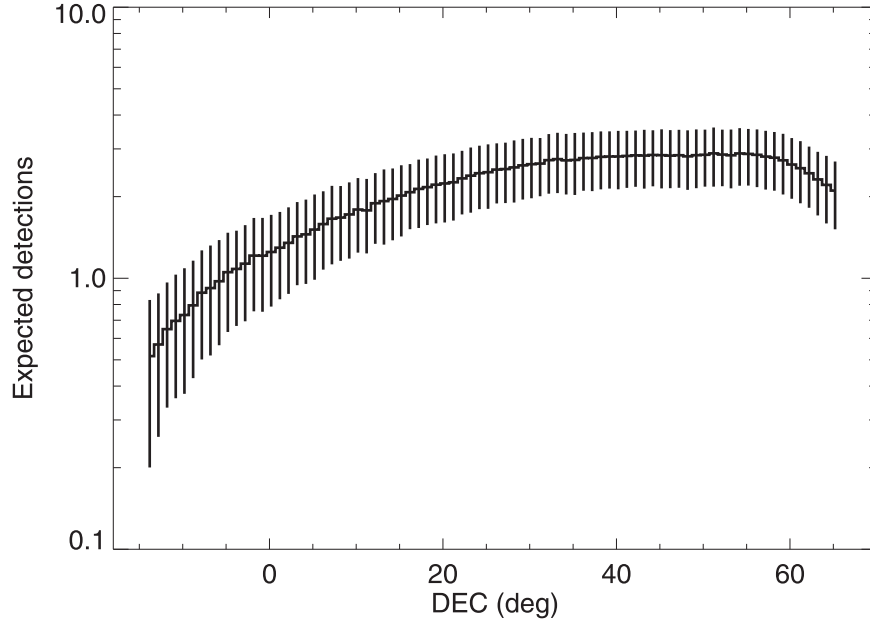
Figure 5. The average number of the flaring UCDs that are expected to be detected during the two-pass drift scans with vertical standard deviation bars obtained from one thousand trials. The decl. bin is 1°.

luminosities following the empirical LF, i.e., $dN/dL \propto L^{-1.96}$ with $L_{\min} = 4.2 \times 10^{23}$ erg s^{-1} (Section 2.3), the rotation periods following the lognormal distribution with $\mu_0 = 1.41$ and $\sigma_0 = 0.48$ (Section 2.4), and the duty cycles uniformly distributed from 0.8% to 35% (Section 2.4).

We randomly select 3% of these objects (Section 2.2), and calculate their flux densities at 1250 MHz (assuming νL_ν is flat). As discussed in Section 2.4, the temporal evolution of the flare can be determined when the peak flux density (F_0), the rotation period (P) and the duty cycle are specified. Here we assume the flaring emission is 100% circularly polarized (Hallinan et al. 2007, 2008; Antonova et al. 2008; Berger et al. 2009; Williams et al. 2015a; Williams & Berger 2015; Route & Wolszczan 2016a). Meanwhile, for the object with given δ, the effective integration time t_{eff} and the corresponding rms noise σ_V are known (see Figures 3 and 4). In this case, we can derive how long the flare lasts with the flux density $\geqslant 5\sigma_V$, which is set as the detection limit. This time duration is denoted by t_{d}. Here σ_V is calculated with t_{eff}, while the total drifting time is approximately $2t_{\mathrm{eff}}$ as noted in Section 3.1. That means when FAST drifts through a source with $2t_{\mathrm{eff}}$, the source should keep in flaring state brighter than $5\sigma_V$. Considering the marginal $5\sigma_V$ detection, $2t_{\mathrm{eff}}$ can be half above and half below $5\sigma_V$ flux limit. Therefore, the probability of each source being detected is $p = t_{\mathrm{d}}/P$. The sources whose $F_0 < 5\sigma_V$ or $t_{\mathrm{d}} < 2t_{\mathrm{eff}}$ are excluded. During the two-pass survey, each point source would be observed twice. The flux variation in Stokes V caused by the flare can be potentially identified, as Stokes V suffers little confusion and gain fluctuation of the system. We calculate the probability of each source being detected once in two

passes, that is, $2p(1-p)$, and add up all the probabilities to obtain the expected value. The average of the expected detections of flaring UCDs in CRAFTS and the corresponding standard deviation at each decl. from a thousand Monte Carlo realizations are shown in Figure 5. The total expected detections are $\sim$170, based on $dN/dL \propto L^{-1.96}$ with $L_{\min} = 4.2 \times 10^{23}$ erg s^{-1}. Considering the uncertainty of the LF power-law index (Section 2.3), we also perform the simulations with $\alpha = 1.51$ and $\alpha = 2.41$. The expected detections are $\sim$500 and $\sim$80, respectively.

4. Discussion

4.1. Alternative Assumptions for the Simulation

In the Monte Carlo simulation, we assume a thin-disk dominated space density distribution of UCDs with a scale height of 300 pc, a 3% flaring UCD detection rate, a radio LF of the flares with a power-law index of 1.96, a flat νL_ν between 1–10 GHz, and a uniform distribution of flare duty cycle from 0.8% to 35%. Under these assumptions, we estimate $\sim$170 flaring UCDs will be detected in CRAFTS. The relevant parameters are chosen mainly to yield a conservative estimate. In the following, we will discuss the uncertainties of these parameters and their impact on the results.

4.1.1. The Scale Height

When we estimate the inhomogeneous spatial distribution of UCDs, we considered the thin disk contribution with a scale height of 300 pc for low-mass stars (Section 3.2). This scale height for brown dwarfs was also measured, but the value
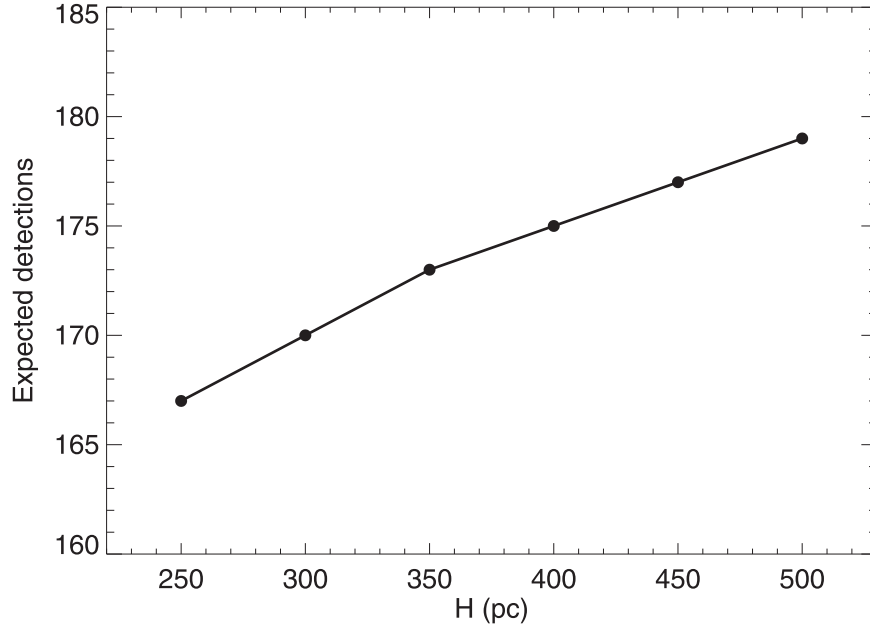
Figure 6. The expected detection number of flaring UCDs during CRAFTS varies with the scale height H of the Galactic thin disk. A larger scale height indicates more UCDs in CRAFTS sky coverage.

suffers from a large uncertainty owing to the faintness of brown dwarfs and the resultant small number statistics. Pirzkal et al. (2005) used six dwarfs with spectral type M4 and later (including two L dwarf candidates) to derive a Galactic disk scale height of 400 ± 100 pc for M and L dwarfs. Ryan et al. (2005) estimated the scale height of 350 ± 50 pc based on 28 L and T dwarfs, and Ryan et al. (2011) drew the value of 290 ± 25 (random) ± 31 (systematic) from 17 newly-discovered UCDs later than M8. Sorahana et al. (2019) detected 3665 L dwarfs and gave a good fit for the scale height of 380 pc.

A scale height larger than the 300 pc adopted here will not significantly affect our results because the maximum visible distance of UCD flares in CRAFTS is only about 180 pc (Figure 4). For the purpose of comparison, we conduct the simulations with different values of the scale height. The results are shown in Figure 6.

4.1.2. The Detection Rate

We derived a detection rate of radio-flaring UCDs to be $\geqslant 3\%$ from a series of unbiased, targeted surveys conducted by both interferometers and single dish telescope in Section 2.2, and adopted the value of 3% in the simulation. Another estimate is referring to the survey detection statistics of Arecibo only, since FAST and Arecibo are both single dish telescopes, and their instrumental properties are similar. They are sensitive to rapidly varying emission, but impractical to detect weak, quiescent emission due to the large beams and the related confusion limitations. In the two surveys of 51 not-previously

detected sources, two flaring dwarfs were seen by Arecibo (Route & Wolszczan 2013, 2016b), yielding a detection rate of $\sim 4\%$. With this value, the expected detection number is 226.

4.1.3. The Spectral Index

Assuming the flux density spectrum of the flare is $S_\nu \propto \nu^\beta$, the spectral index β would affect the simulation significantly. The measurements of spectral indices are limited, as the multi-band simultaneous radio observations are unusual. Williams et al. (2017) observed WISEP J1122+2550 using VLA at 4–8 GHz. They generated two images by splitting the 4 GHz bandwidth into halves with central frequencies of 5.00 and 7.00 GHz, and implied $\beta = -1.5 \pm 0.3$. It can be taken as the spectral index of flaring emission, as they considered there may be no quiescent emission in this dwarf. Kao et al. (2018) used VLA to observe four radio-emitting brown dwarfs at 8–12 GHz and one at 12–18 GHz. For those observed at 8–12 GHz, we adopt pulse flux densities at sub-bands 8–10 and 10–12 GHz with central frequencies of 9.00 and 11.00 GHz, and estimate $\beta = -1.7 \pm 1.3$ for SIMP J0136+0933 and $\beta = -1.4 \pm 0.8$ for 2MASS 1043+2225 (see Table 7 in Kao et al. (2018), values in "All Pulses" column are adopted for 2MASS 1043+2225). For 2MASS 1237+6526, there are three pulses (see Table 5 in Kao et al. 2018), and $\beta = 2.0 \pm 1.7$, 0.7 ± 0.4 and 1.5 ± 0.9, respectively. For SDSS 0423-0414, there are two right-circularly polarized pulses, labeled as Pulse R1 and R2, and four left-circularly polarized pulses, labeled as Pulse L1, L2, L3 and L4 (see Table 8 in Kao et al. 2018). For Pulse L2 and L4,
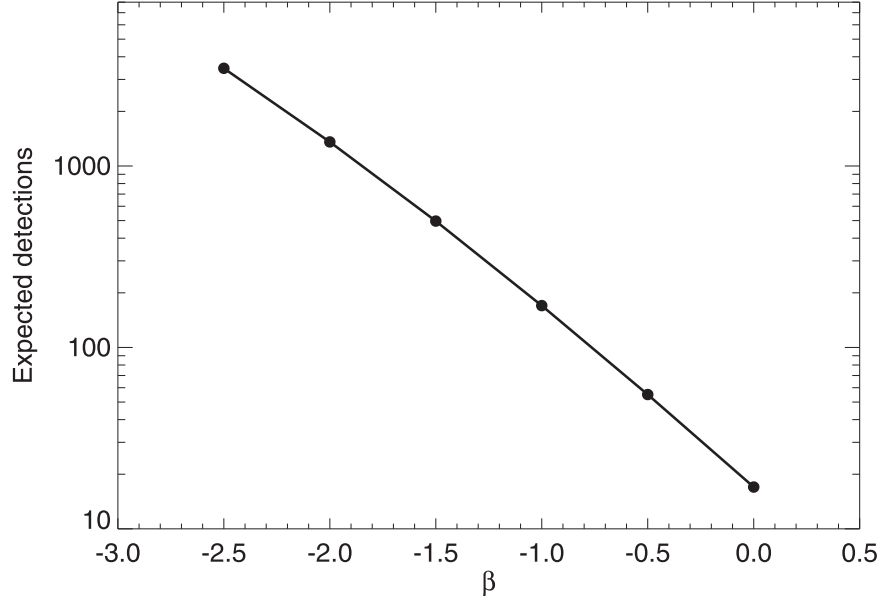
Figure 7. The expected detection number of flaring UCDs during CRAFTS varies with the spectral index β of the flaring emission. A more negative value of β implies a stronger L-band flux. The visible distance of UCD flares in CRAFTS thus extends further, and the detection number increases as a result.

pulses are detectable at 8–10 GHz, but not at 10–12 GHz. It may be a hint of ECM emission frequency cutoff. Thus we calculate spectral indices for another four pulses and $\beta = -0.4 \pm 1.1$, -2.7 ± 1.3, -2.9 ± 1.1 and -2.2 ± 0.9, respectively. In addition, 2MASS 1047+2124 was observed at 12–18 GHz, and six pulses were detected. The 6 GHz bandwidth is divided into four sub-bands. These pulses were detectable in one sub-band at most, except Pulse 5 (see Table 6 in Kao et al. 2018). For this pulse, considering the flux densities of 93.7 ± 24.0 μJy at 15.75 GHz and 91.5 ± 28.7 μJy at 17.25 GHz, the spectral index is $\beta = -0.3 \pm 4.4$.

On the other hand, from the perspective of ECM theory, electrons are accelerated in the magnetic field-aligned electric fields. Under the mirror effect of the converging magnetic field-lines, the energy gained in the electric fields is transferred from parallel to perpendicular energy (with respect to the magnetic field). The resulting electron-velocity distribution is unstable. Its positive gradient in the perpendicular velocity leads to the exponential growth of the radiation. The intensity of ECM emission depends on the magnetic field strength and structure, the electron density and energy distribution, the electron-distribution function in velocity space and the radiation source region size (Treumann 2006). Observed ECM emissions at different frequencies are considered to originate from source regions at different heights over the surface. Their flux densities are not predictable, as not all aforementioned parameters in localized source regions are known.

In this work we assume $\beta = -1.0$, that is, νL_ν is flat, and consider other values ranging from -2.5 to 0 with a step of 0.5 to investigate the effect of β on the simulation. This

assumption is not unreasonable. In the above-mentioned seven cases, the spectral indices of WISEP J1122+2550, SIMP J0136+0933 and 2MASS 1043+2225 are between -1.0 and -2.0, while the median value of SDSS 0423-0414 is steeper. If taking into account the uncertainties, $\beta = -1.0$ is applicable to these objects and also 2MASS 1047+2124. Moreover, Vedantham et al. (2020) discovered BDR J1750 +3809 at around 144 MHz with a radio spectral luminosity of $\sim 5 \times 10^{15}$ erg s^{-1} Hz^{-1}. The radio luminosity is $\nu L_\nu \approx 7.2 \times 10^{23}$ erg s^{-1}, consistent with the values listed in Table 1. It is worth noting that Kao et al. (2018) found pulses that seem more intermittent at high frequencies. They proposed one possibility that while large-scale fields are necessary to drive auroral currents to produce radio flaring emissions, small-scale fields may emerge near the surface of the object, causing rapid variation of pulses in both time and frequency. This phenomenon begins to appear around 10 GHz for SDSS 0423-0414 and seems more obvious above 12 GHz in the case of 2MASS 1047+2124. As the origin of this phenomenon is unclear yet, we note that it is safer to apply the assumption of flat νL_ν to radio emissions below 10 GHz.

The simulation results with different values of β are shown in Figure 7. When $\beta = 0$, <20 radio-flaring UCDs would be detected. A more negative value of β yields more expected detections, as the inferred L-band flux would be higher. If a more extreme $\beta = -2.5$ is considered, the expected detection number would increase dramatically to $\sim$3460, one order of magnitude larger than that predicted from $\beta = -1.0$. Thus the future survey results would help constrain the average spectral index.

4.1.4. The LF Index

When we derived the LF index α in Section 2.3, we follow Clauset et al. (2009) to normalize the constant k by integrating to infinity. In reality, the probability would be zero at the luminosity higher than the most luminous event ($L_{\max}$) (Aschwanden 2015), and thus the normalization should be written as $k = (\alpha - 1)/(L_{\min}^{-\alpha+1} - L_{\max}^{-\alpha+1})$. The existence of $L_{\max}$ makes the LF flatter. Without further knowledge of $L_{\max}$ from limited surveys on UCD flares, here we consider an extreme case that it is the currently observed maximal luminosity, that is, $L_{\max} = 4.92 \times 10^{24}$ erg s^{-1}. By maximizing Equation (2), we obtain $\alpha = 1.37$. The expected detection number of flaring UCDs is $\sim$100. For more comparison, we also run the simulation with $L_{\max} = 9.84 \times 10^{24}$ erg s^{-1} and the corresponding $\alpha = 1.69$. The result is $\sim$130.

4.2. Confirmation of Flaring UCD Candidates

When we use the Stokes V flux difference between two-pass observations to search for radio-flaring UCDs, the sample will be contaminated by other radio sources with variability. Apart from UCDs and planets, the known radio transients emitting the continuum with high circular polarization are stars (earlier than M7) and pulsars. Cross-matching the archival information about that source on the sky would be helpful for early identification. By this means Pritchard et al. (2021) identified 33 radio stars in the Rapid ASKAP Continuum Survey (RACS) and Callingham et al. (2021) reported radio detection of 19 M dwarfs in LoTSS with $\approx$20% of the Northern sky processed. The catalog of brown dwarfs is far from complete in the solar neighborhood so far, yet it will be greatly improved in future infrared surveys, e.g., Euclid, SPHEREx and Roman. Moreover, we need the follow-up observation for confirmation and detailed studies, especially for those distant and faint objects, which could be beyond the scope of other radio telescopes.

The strategy of selecting flaring UCD candidates in CRAFTS mainly depends on two factors: the available tracking time of the target and the corresponding FAST sensitivity. The top plot in Figure 8 shows the maximum tracking time for a target depending on its decl. The sources with the decl. between 3°.4 and 49°.2 can be observed continuously for at least 2 h when keeping $ZA \leqslant 26°.4$. If $ZA > 26°.4$ (with reduced sensitivity) is acceptable, the 2 h long observation would be available to the sources with the decl. from $-11°.7$ to 64°.4. The bottom plot in Figure 8 shows the sensitivity variation of the telescope in Stokes V with ZA when FAST works in tracking mode. The sensitivity in a single polarization is calculated by Equation (5) with the reported gain and system temperature at different frequencies in Jiang et al. (2020), and the average is adopted over the frequency. The sensitivity in Stokes V is $\sqrt{2}$ times larger than this value. When tracking the sources with the decl. below $-0°.7$ or above 52°.1, the minimum ZA is 26°.4. That means the best sensitivity in Stokes V (with 10 s time

resolution for reference in Figure 8) is $\sim$41.0 μJy, reduced by approximately 31% compared to the value of $\sim$31.2 μJy near $ZA = 0°$, and the sensitivity decreases quickly with increasing ZA. For these sources, a more sophisticated observation scheme should be designed to compensate the sensitivity requirement and the continuous flux monitoring duration.

4.3. Implication of Flaring UCD Search in L-band Survey

Since radio-active UCDs were discovered at $\sim$5 GHz and $\sim$8 GHz, as summarized in Section 2.1, lower frequency observations have been attempted to explore the nature of the radio emission at low frequencies. Osten et al. (2006) conducted VLA observations of TVLM 513-46 at 8.4, 4.8 and 1.4 GHz. They detected persistent radio emission at all frequencies, yet no flares. Later Osten et al. (2009) observed another two radio sources 2MASS J0523-1403 and LHS 3003 at these three frequencies, and no radio emission was detected. McLean et al. (2011) detected quiescent emission of $\sim$1 mJy at 1.43, 4.86, 8.46 and 22.5 GHz from 2MASS J1314+1320 with VLA. Metodieva et al. (2017) used the upgraded VLA to observe six radio-emitting UCDs at S (2–4 GHz) and C (4–7 GHz) band. Quiescent radio emissions were detected from five sources at both bands, while the flaring emission was only detected from LSR J1835+3259 at S band. This was the first time that a flare below $\sim$4 GHz was detected from a UCD. Moreover, Zic et al. (2019) presented the results of nine UCDs observed by GMRT at $\sim$610 and $\sim$1300 MHz. Only quiescent emissions were detected from 2MASS J1314+1320 and 2MASS J0746+2000 at these two frequencies. Hundreds of MHz observations of UCDs were also carried out. Unfortunately, neither VLA observations of two UCDs at 325 MHz (Jaeger et al. 2011) nor LOFAR mini-survey of three UCDs at around 140 MHz (Burningham et al. 2016) detected any radio emission. Though non-detection from target objects, Vedantham et al. (2020) discovered a circularly polarized radio source at around 144 MHz in LoTSS. Follow-up near-infrared observations confirmed that it is a T6.5 brown dwarf at a distance of 65 pc. This is the first radio-discovered brown dwarf. In view of the high brightness temperature and circular fraction, the detected radio emission is interpreted as ECM emission, and the field strength of this object is inferred to be at least 25 Gauss.

The effort on low frequency exploration, though appreciated, is far from enough. As the flaring emission at $\sim$1 GHz has not been detected from any UCD yet, our understanding of the nature of such emission is limited. ECM emission is radiated mostly at the fundamental and the second harmonic of electron-cyclotron frequency, $\nu_c = eB/2\pi m_e c \approx 2.8 \times B$ [MHz]. Thus the observed flaring emission can be used to measure the local magnetic field, and 1.4 GHz emission corresponds to a magnetic field of 250–500 Gauss. It could be the case: (1)
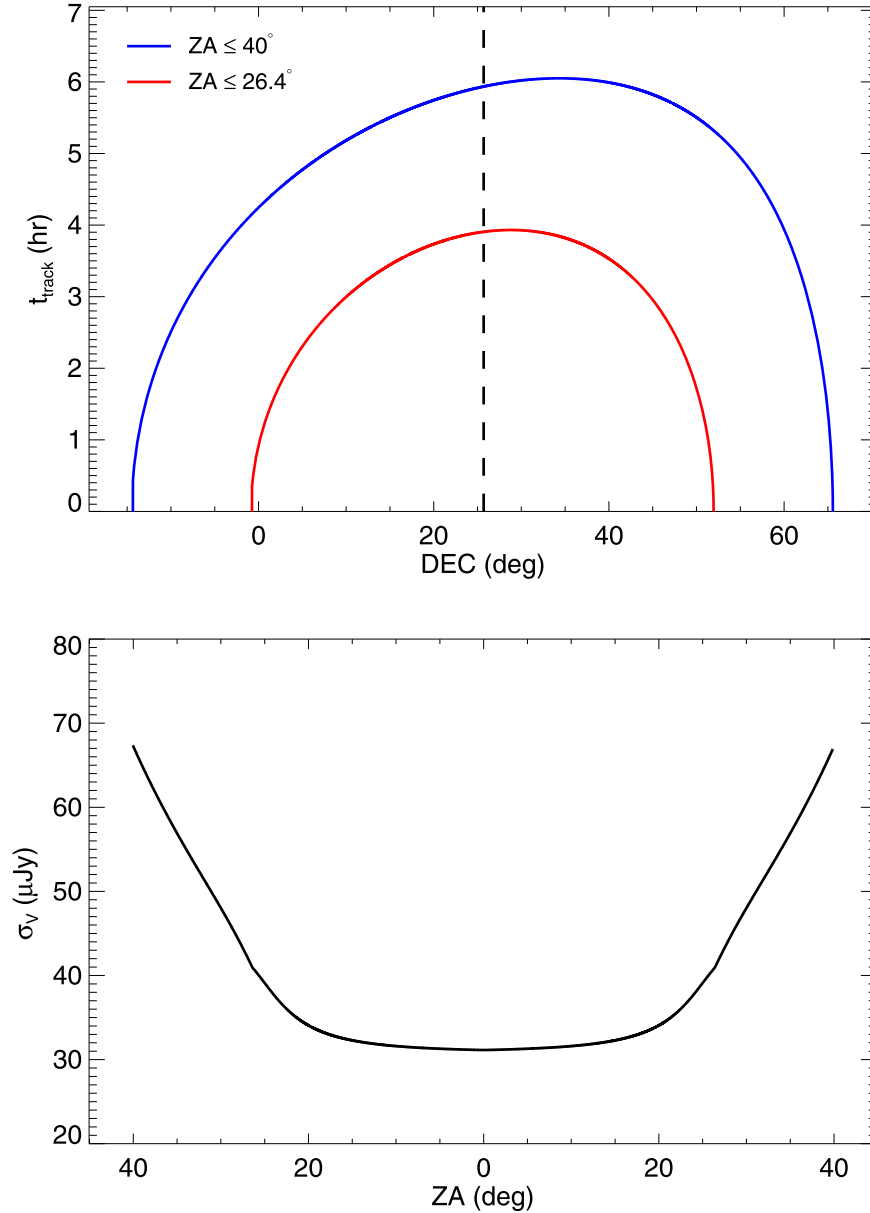
Figure 8. Top: Maximum tracking time vs. target decl. when *ZA* is below 40° (blue) and 26°.4 (red). The dashed line marks the latitude of FAST. This plot is from Jiang et al. (2020). Bottom: The rms noise in Stokes *V* when tracking as a function of *ZA* with 10 s time resolution for reference.

the source region with this field strength is located at a certain height over the surface of an object where the field strength is stronger and (2) this is the maximum surface field strength of an object. As mentioned in Section 1, Christensen et al. (2009) proposed an energy flux scaling law working from rapidly rotating low-mass stars to solar system planets. Based on this scaling law, Reiners et al. (2009) expressed the field strength in terms of mass M, luminosity L and radius R, that is, $B = 4.8 \times (ML^2/R^7)^{1/6}$ [kG] with all parameters normalized with solar values. Further Reiners & Christensen (2010) calculated the evolution of average magnetic fields in brown

dwarfs and exoplanets. They claimed that magnetic fields in brown dwarfs and planets weaken over time as they become fainter, losing luminosity which is the power source of magnetic field generation. According to the calculation (see Figure 1 in Reiners & Christensen 2010), a $5M_J$ planet is predicted to have a polar dipole field strength of ∼500 Gauss during the first few million years, and a brown dwarf with $M = 25M_J$ can maintain an average surface field of ∼250 Gauss after 10 Gyr. Objects with masses between them would own surface magnetic fields of 250–500 Gauss for some time during their lifetime. Flaring UCD search in *L*-band survey is expected

to find such objects including exoplanets. Alternatively, Kao et al. (2018) found that late L dwarfs marginally follow the energy flux scaling law, and T dwarfs clearly depart from it based on studies of five targets. Radio-flaring UCDs and planets with diverse masses, luminosities and radii discovered in the survey can be used to test this scaling law. For instance, assuming a $\sim 10 M_J$ ($0.01 M_\odot$) planet with a radius of $\sim 1 R_J$ ($0.1 R_\odot$) was discovered in the survey, it meant the field strength of this object was at least ~ 500 Gauss, considering the fundamental electron-cyclotron frequency. If its luminosity was much smaller than $L = \sqrt{(B/4.8)^6 R^7 / M} \approx 3.6 \times 10^{-6} L_\odot$, it could be considered to deviate from the energy flux scaling law. Infrared data are needed to derive these physical parameters. Note that this luminosity-driven dynamo is tenable for dipole-dominated fields in fast rotators whose rotation rate is above some threshold value and field strength is independent of rotation rate. For objects that rotate not fast enough for dynamo saturation, their field strengths and topologies depend on rotation (Chabrier & Küker 2006; Dobler et al. 2006; Browning 2008). New sample discovered in the survey with different rotation rates would be helpful to investigate the influence of rotation on the dynamos.

5. Conclusions

In this paper, we evaluate the capabilities of FAST to detect radio-flaring UCDs during the two-pass drift-scan survey CRAFTS. In the previous surveys, the overall detection rate of radio-active UCDs is $\sim 10\%$. Compiling the data from a number of unbiased, targeted radio surveys, we have estimated a flaring UCD detection rate of $\geqslant 3\%$, and constructed a flare luminosity function $dN/dL \propto L^{-1.96 \pm 0.45}$ (here $L = \nu L_\nu$).

The most luminous radio flare detected in these surveys is from DENIS J1048-3956 with $\nu L_\nu = 4.92 \times 10^{24}$ erg s^{-1}. The similar flaring events can be seen by CRAFTS up to ~ 180 pc at 1250 MHz. Taking into account the spatial distribution of these dwarfs with a scale height of 300 pc, we have performed a Monte Carlo simulation to generate mock catalog with distances, radio luminosities, rotation periods and flare duty cycles, which contains $\sim 3.26 \times 10^5$ UCDs in the CRAFTS sky coverage. Adopting the aforementioned $\sim 3\%$ flaring UCD fraction, we have estimated that ~ 170 dwarfs are expected to be detected as transients, assuming 100% circularly polarized emission. Radio-flaring UCDs discovered in the survey would gain our understanding of UCD behavior at L band and dynamos.

While a giant single dish telescope such as FAST has the advantage to detect faint radio flares at low frequencies, the radio interferometers can detect slowly varying radio emission that is not accessible to the single dish due to its large beam size and other practical limitations. Together with the forth-coming SKA, these two complementary, world-class telescopes

are expected to shed light on the magnetic fields and dynamos of UCDs.

References

Allers, K. N., Vos, J. M., Biller, B. A., & Williams, P. K. G. 2020, Sci, 368, 169
Antonova, A., Doyle, J. G., Hallinan, G., Bourke, S., & Golden, A. 2008, A&A, 487, 317
Antonova, A., Hallinan, G., Doyle, J. G., et al. 2013, A&A, 549, A131
Aschwanden, M. J. 2015, ApJ, 814, 19
Bardalez Gagliuffi, D. C., Burgasser, A. J., Schmidt, S. J., et al. 2019, ApJ, 883, 205
Becker, R. H., White, R. L., & Helfand, D. J. 1995, ApJ, 450, 559
Berger, E. 2002, ApJ, 572, 503
Berger, E. 2006, ApJ, 648, 629
Berger, E., Ball, S., Becker, K. M., et al. 2001, Natur, 410, 338
Berger, E., Basri, G., Fleming, T. A., et al. 2010, ApJ, 709, 332
Berger, E., Rutledge, R. E., Phan-Bao, N., et al. 2009, ApJ, 695, 310
Best, W. M. J., Magnier, E. A., Liu, M. C., et al. 2018, ApJS, 234, 1
Binney, J., Gerhard, O., & Spergel, D. 1997, MNRAS, 288, 365
Bochanski, J. J., Hawley, S. L., Covey, K. R., et al. 2010, AJ, 139, 2679
Bouy, H., Duchêne, G., Köhler, R., et al. 2004, A&A, 423, 341
Browning, M. K. 2008, ApJ, 676, 1262
Burgasser, A. J., Geballe, T. R., Leggett, S. K., Kirkpatrick, J. D., & Golimowski, D. A. 2006, ApJ, 637, 1067
Burgasser, A. J., Melis, C., Todd, J., et al. 2015, AJ, 150, 180
Burgasser, A. J., Melis, C., Zauderer, B. A., & Berger, E. 2013, ApJL, 762, L3
Burgasser, A. J., & Putman, M. E. 2005, ApJ, 626, 486
Burningham, B., Hardcastle, M., Nichols, J. D., et al. 2016, MNRAS, 463, 2202
Callingham, J. R., Vedantham, H. K., Shimwell, T. W., et al. 2021, NatAs, 5, 1233
Chabrier, G., & Küker, M. 2006, A&A, 446, 1027
Christensen, U. R., Holzwarth, V., & Reiners, A. 2009, Natur, 457, 167
Clauset, A., Shalizi, C. R., & Newman, M. E. J. 2009, SIAMR, 51, 661
Cohen, M. 1995, ApJ, 444, 874
Condon, J. J., Cotton, W. D., Greisen, E. W., et al. 1998, AJ, 115, 1693
Dobler, W., Stix, M., & Brandenburg, A. 2006, ApJ, 638, 336
Dupuy, T. J., & Liu, M. C. 2017, ApJS, 231, 15
Filippazzo, J. C., Rice, E. L., Faherty, J., et al. 2015, ApJ, 810, 158
Gaia Collaboration, Brown, A. G. A., Vallenari, A., et al. 2018, A&A, 616, A1
Gizis, J. E., Burgasser, A. J., Berger, E., et al. 2013, ApJ, 779, 172
Gizis, J. E., Monet, D. G., Reid, I. N., et al. 2000, AJ, 120, 1085
Gizis, J. E., Williams, P. K. G., Burgasser, A. J., et al. 2016, AJ, 152, 123
Guirado, J. C., Azulay, R., Gauza, B., et al. 2018, A&A, 610, A23
Hallinan, G., Antonova, A., Doyle, J. G., et al. 2006, ApJ, 653, 690
Hallinan, G., Antonova, A., Doyle, J. G., et al. 2008, ApJ, 684, 644
Hallinan, G., Bourke, S., Lane, C., et al. 2007, ApJL, 663, L25
Hallinan, G., Littlefair, S. P., Cotter, G., et al. 2015, Natur, 523, 568
Harding, L. K., Hallinan, G., Konopacky, Q. M., et al. 2013, A&A, 554, A113
Heiles, C. 2001, PASP, 113, 1243

Heiles, C., Perillat, P., Nolan, M., et al. 2001, PASP, 113, 1274
Henry, T. J., Subasavage, J. P., Brown, M. A., et al. 2004, AJ, 128, 2460
Jaeger, T. R., Osten, R. A., Lazio, T. J., Kassim, N., & Mutel, R. L. 2011, AJ, 142, 189
Jiang, P., Tang, N.-Y., Hou, L.-G., et al. 2020, RAA, 20, 064
Jiang, P., Yue, Y., Gan, H., et al. 2019, SCPMA, 62, 959502
Jurić, M., Ivezić, Ž., Brooks, A., et al. 2008, ApJ, 673, 864
Kao, M. M., Hallinan, G., Pineda, J. S., et al. 2016, ApJ, 818, 24
Kao, M. M., Hallinan, G., & Pineda, J. S. 2019, MNRAS, 487, 1994
Kao, M. M., Hallinan, G., Pineda, J. S., Stevenson, D., & Burgasser, A. 2018, ApJS, 237, 25
Kerr, F. J., & Lynden-Bell, D. 1986, MNRAS, 221, 1023
Kirkpatrick, J. D., Cushing, M. C., Gelino, C. R., et al. 2011, ApJS, 197, 19
Kirkpatrick, J. D., Henry, T. J., & Simons, D. A. 1995, AJ, 109, 797
Kirkpatrick, J. D., Martin, E. C., Smart, R. L., et al. 2019, ApJS, 240, 19
Kirkpatrick, J. D., Reid, I. N., Liebert, J., et al. 1999, ApJ, 519, 802
Kirkpatrick, J. D., Reid, I. N., Liebert, J., et al. 2000, AJ, 120, 447
Leggett, S. K., Allard, F., Geballe, T. R., Hauschildt, P. H., & Schweitzer, A. 2001, ApJ, 548, 908
Li, D., Wang, P., Qian, L., et al. 2018, IMMag, 19, 112
Lynch, C., Murphy, T., Ravi, V., et al. 2016, MNRAS, 457, 1224
Lynch, C., Mutel, R. L., & Güdel, M. 2015, ApJ, 802, 106
McLean, M., Berger, E., Irwin, J., Forbrich, J., & Reiners, A. 2011, ApJ, 741, 27
McLean, M., Berger, E., & Reiners, A. 2012, ApJ, 746, 23
Metchev, S. A., Heinze, A., Apai, D., et al. 2015, ApJ, 799, 154
Metodieva, Y. T., Kuznetsov, A. A., Antonova, A. E., et al. 2017, MNRAS, 465, 1995
Mohanty, S., & Basri, G. 2003, ApJ, 583, 451
Ng, Y. K., Bertelli, G., Chiosi, C., & Bressan, A. 1997, A&A, 324, 65
Osten, R. A., Hawley, S. L., Bastian, T. S., & Reid, I. N. 2006, ApJ, 637, 518
Osten, R. A., & Jayawardhana, R. 2006, ApJL, 644, L67
Osten, R. A., Melis, C., Stelzer, B., et al. 2015, ApJL, 805, L3
Osten, R. A., Phan-Bao, N., Hawley, S. L., Reid, I. N., & Ojha, R. 2009, ApJ, 700, 1750
Parker, E. N. 1975, ApJ, 198, 205
Phan-Bao, N., Osten, R. A., Lim, J., Martín, E. L., & Ho, P. T. P. 2007, ApJ, 658, 553
Pineda, J. S., Hallinan, G., & Kao, M. M. 2017, ApJ, 846, 75
Pineda, J. S., Hallinan, G., Kirkpatrick, J. D., et al. 2016, ApJ, 826, 73
Pirzkal, N., Burgasser, A. J., Malhotra, S., et al. 2009, ApJ, 695, 1591
Pirzkal, N., Sahu, K. C., Burgasser, A., et al. 2005, ApJ, 622, 319
Pritchard, J., Murphy, T., Zic, A., et al. 2021, MNRAS, 502, 5438

Radigan, J., Lafrenière, D., Jayawardhana, R., & Artigau, E. 2014, ApJ, 793, 75
Reiners, A., & Basri, G. 2008, ApJ, 684, 1390
Reiners, A., Basri, G., & Christensen, U. R. 2009, ApJ, 697, 373
Reiners, A., & Christensen, U. R. 2010, A&A, 522, A13
Reylé, C., Delorme, P., Willott, C. J., et al. 2010, A&A, 522, A112
Richey-Yowell, T., Kao, M. M., Pineda, J. S., Shkolnik, E. L., & Hallinan, G. 2020, ApJ, 903, 74
Route, M. 2016, ApJL, 830, L27
Route, M. 2017, ApJ, 845, 66
Route, M., & Wolszczan, A. 2012, ApJL, 747, L22
Route, M., & Wolszczan, A. 2013, ApJ, 773, 18
Route, M., & Wolszczan, A. 2016a, ApJL, 821, L21
Route, M., & Wolszczan, A. 2016b, ApJ, 830, 85
Route, M. P. 2013, PhD thesis, The Pennsylvania State University
Ryan, R. E., Thorman, P. A., Yan, H., et al. 2011, ApJ, 739, 83
Ryan, R. E. J., Hathi, N. P., Cohen, S. H., & Windhorst, R. A. 2005, ApJ, 631, L159
Schmidt, S. J., Hawley, S. L., West, A. A., et al. 2015, AJ, 149, 158
Shimwell, T. W., Röttgering, H. J. A., Best, P. N., et al. 2017, A&A, 598, A104
Shimwell, T. W., Tasse, C., Hardcastle, M. J., et al. 2019, A&A, 622, A1
Sorahana, S., Nakajima, T., & Matsuoka, Y. 2019, ApJ, 870, 118
Treumann, R. A. 2006, A&ARv, 13, 229
Vedantham, H. K., Callingham, J. R., Shimwell, T. W., et al. 2020, ApJL, 903, L33
Vrba, F. J., Henden, A. A., Luginbuhl, C. B., et al. 2004, AJ, 127, 2948
West, A. A., Hawley, S. L., Walkowicz, L. M., et al. 2004, AJ, 128, 426
Williams, P. K. G., & Berger, E. 2015, ApJ, 808, 189
Williams, P. K. G., Berger, E., Irwin, J., Berta-Thompson, Z. K., & Charbonneau, D. 2015a, ApJ, 799, 192
Williams, P. K. G., Casewell, S. L., Stark, C. R., et al. 2015b, ApJ, 815, 64
Williams, P. K. G., Berger, E., & Zauderer, B. A. 2013, ApJL, 767, L30
Williams, P. K. G., Cook, B. A., & Berger, E. 2014, ApJ, 785, 9
Williams, P. K. G., Gizis, J. E., & Berger, E. 2017, ApJ, 834, 117
Yadav, R. K., Christensen, U. R., Morin, J., et al. 2015, ApJL, 813, L31
Zapatero Osorio, M. R., Martín, E. L., Bouy, H., et al. 2006, ApJ, 647, 1405
Zhang, K., Wu, J., Li, D., et al. 2019, SCPMA, 62, 959506
Zhang, Q., Hallinan, G., Brisken, W., Bourke, S., & Golden, A. 2020, ApJ, 897, 11
Zic, A., Lynch, C., Murphy, T., Kaplan, D. L., & Chandra, P. 2019, MNRAS, 483, 614